

U-ViLAR: Uncertainty-Aware Visual Localization for Autonomous Driving via Differentiable Association and Registration

Xiaofan Li*, Zhihao Xu*, Chenming Wu, Zhao Yang, Yumeng Zhang, Jiang-Jiang Liu, Haibao Yu, Fan Duan, Xiaoqing Ye, Yuan Wang, Shirui Li, Xun Sun, Ji Wan, Jun Wang
Baidu Inc.

Abstract

Accurate localization using visual information is a critical yet challenging task, especially in urban environments where nearby buildings and construction sites significantly degrade GNSS (Global Navigation Satellite System) signal quality. This issue underscores the importance of visual localization techniques in scenarios where GNSS signals are unreliable. This paper proposes U-ViLAR, a novel uncertainty-aware visual localization framework designed to address these challenges while enabling adaptive localization using high-definition (HD) maps or navigation maps. Specifically, our method first extracts features from the input visual data and maps them into Bird’s-Eye-View (BEV) space to enhance spatial consistency with the map input. Subsequently, we introduce: **a) Perceptual Uncertainty-guided Association**, which mitigates errors caused by perception uncertainty, and **b) Localization Uncertainty-guided Registration**, which reduces errors introduced by localization uncertainty. By effectively balancing the coarse-grained large-scale localization capability of association with the fine-grained precise localization capability of registration, our approach achieves robust and accurate localization. Experimental results demonstrate that our method achieves state-of-the-art performance across multiple localization tasks. Furthermore, our model has undergone rigorous testing on large-scale autonomous driving fleets and has demonstrated stable performance in various challenging urban scenarios.

1. Introduction

Autonomous vehicles rely significantly on Global Navigation Satellite Systems (GNSS) for outdoor localization. However, GNSS signals are susceptible to noise caused by obstructions from buildings, tunnels, and bridges, which complicates the accuracy of GNSS-based localization. In

*Equal contribution.

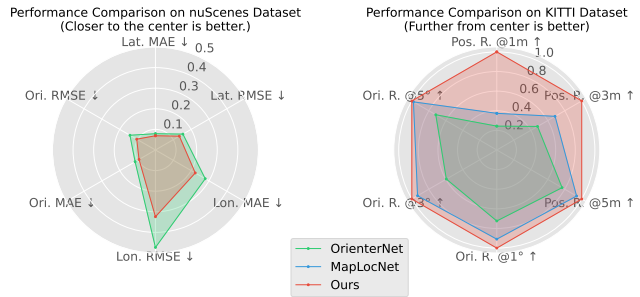


Figure 1. In **Fine-grained Localization (left)** and **Large-scale Relocalization (right)**, U-ViLAR outperforms all existing methods across all metrics. Lat., Lon., and Ori. represent Lateral, Longitudinal, and Orientation, respectively, while R. denotes Recall.

this context, visual localization using imprecise GNSS data is becoming increasingly critical. In autonomous driving systems, localization typically demands centimeter-level accuracy [2], whether using high-definition (HD) maps or lightweight navigation maps. Both types of maps are crucial for autonomous driving due to their precision or cost-effectiveness. In this regard, an end-to-end visual localization system that can adapt to both map types and coarse GNSS signals is essential.

Classical methods for visual localization rely on establishing 2D-3D correspondences between keypoint visual descriptors in images and 3D points in Structure-from-Motion (SfM) models. Traditional image feature extraction techniques, such as SIFT [29], SURF [3], ORB [36], FREAK [1, 4], and BRIEF [6, 25], tend to perform poorly under significant changes in viewpoint or illumination. Although learnable features like SuperPoint [9], R2D2 [34], and GIFT [26] have enhanced robustness to some extent, they still face challenges with variations in weather and appearance. Moreover, constructing large-scale 3D maps is highly expensive, and these maps require frequent updates to reflect environmental changes. The cost of storing 3D maps in vehicles further complicates their implementation in city-scale areas.

Recent approaches have transitioned from relying exclusively on appearance information to incorporating semantic data for localization in vectorized maps. These methods generally extract semantic features using pre-trained convolutional neural networks (CNNs) and then link these features through filtering or optimization techniques to achieve precise localization. However, semantic features can be affected by artifacts or missing data, prompting the use of complex handcrafted strategies like graph matching [45] or distance transforms [31]. These approaches often require careful tuning of various hyperparameters, making them cumbersome and difficult to generalize. Notable works, such as BEV-Locator [49], focus on centimeter-level localization using HD maps, attempting to directly regress pose offsets with transformer-based models that jointly encode image and map features. Nonetheless, the absence of explicit geometric constraints results in limited accuracy and robustness in direct pose regression. OrienterNet [39], designed for relocalization using navigation maps, introduces explicit 3-DoF (Degree-of-Freedom) pose probability modeling after fusing image and map features but still lacks clear modeling of matching relationships in BEV space. MapLocNet [47] enhances OrienterNet’s performance with a coarse-to-fine pose regression model but does not address explicit image-map matching.

To tackle the issues present in existing methods, this paper presents an uncertainty-aware, end-to-end visual localization framework that enables adaptive localization across different map formats by integrating matching and search strategies. Specifically, drawing inspiration from end-to-end image feature matching [38,44], we establish both global and local associations between image features and BEV map features to create cross-modal relationships. Our design uniquely incorporates perceptual uncertainty as a guiding mechanism, leveraging multivariate Gaussian for global supervision and contrastive learning to enhance local association robustness. Unlike traditional methods that optimize poses based on matches, we employ a pose decoder to regress pose distributions. This approach constructs refined solution spaces centered around coarse localization uncertainty, enabling the search for precise poses. By integrating these strategies, our method effectively combines the large-scale localization capabilities of matching with the fine-grained precision of registration within localized regions. Our contributions can be summarized as follows:

- We introduce a novel uncertainty-aware progressive visual localization framework, supporting various map formats and localization tasks.
- We propose Perceptual Uncertainty-guided Association, which integrates perception uncertainty into probabilistic modeling, to reduce the impact of low-quality regions.

- We propose Localization Uncertainty-guided Registration, leveraging coarse pose uncertainty as a prior for fine-grained localization, addressing non-unimodal pose distribution challenges.
- Extensive experiments on centimeter-level localization in small areas and large-scale relocalization demonstrate that our proposed U-ViLAR achieves state-of-the-art performance across various datasets.

2. Related Work

2.1. BEV Representation in Visual Perception

Transforming image features into BEV space can be achieved through geometric or learning-based methods. Geometric approaches, such as Cam2BEV [33] and VectorMapNet [28], apply Inverse Perspective Mapping (IPM) to convert image features into BEV grids. Learning-based methods, such as LSS [32], predict depth to project image pixels into BEV space, further refined by BEVDet [16] and BEVDepth [21] for improved 3D perception. Alternative approaches include query-based models like Detr3D [46], which sample image features using 3D queries for regression, and GitNet [12], which introduces a two-stage perspective-to-BEV transformation. Recent methods, such as BEVFormer [23] and PETR [27], leverage cross-attention and 3D position encoding to enhance 2D-to-BEV mapping.

2.2. Visual Localization

Traditional localization methods rely on geometric feature matching, using hand-crafted descriptors such as SIFT, SURF, and ORB to associate 2D image pixels with 3D scene points [22,42]. However, these methods are sensitive to viewpoint and illumination variations. Deep learning improves robustness by replacing handcrafted features with learned representations [9,34], yet computational costs remain high. Semantic maps provide stable environmental cues such as lane markings and poles, enabling localization through LiDAR-based map matching [19,20] and neural-based pose estimation [17]. Further improvements integrate sensor fusion [43] and monocular SLAM [40], enhancing accuracy and robustness. Large-scale localization has shifted towards lightweight navigation maps, where semantic matching between urban images and 2D maps [30,37] facilitates positioning. Cross-view approaches [10,18] align ground-level and aerial imagery, while OrienterNet [39] achieves sub-meter precision using BEV-based neural matching with OpenStreetMap [13].

2.3. End-to-End Localization

End-to-end (E2E) localization methods directly infer poses from sensor inputs and prior maps, eliminating the need for explicit matching. PixLoc [24] introduces a differentiable optimization framework, aligning depth features

with a reference 3D model to estimate poses in an E2E manner. I2D-Loc [8] further enhances efficiency by integrating local image-LiDAR depth registration and BPnP-based gradient computation for pose refinement. More recent advancements, such as BEV-Locator [49], leverage multi-view images and vectorized global maps, employing a cross-modal Transformer to align semantic map elements with camera images. EgoVM [15] extends this paradigm by achieving centimeter-level localization by integrating point cloud data and lightweight vectorized maps. However, although these methods can output localization results end-to-end, they tend to be relatively simplistic and lack fine precision. We designed the model structure based on priors from the localization domain while ensuring gradient continuity, achieving performance that far surpasses previous work.

3. Method

Problem Definition. Given an initial estimate $\mathbf{P}_0 = (x_0, y_0, \varphi_0)^\top \in \mathbb{R}^3$ obtained from noisy sensor measurements, our objective is to predict a minimal correction $\Delta\mathbf{P} = (\delta x, \delta y, \delta\varphi)$ that aligns this estimate with the ground-truth pose $\mathbf{P}_{\text{gt}} \in \mathbb{R}^3$. This correction is expressed as a rigid-body transformation in the Special Euclidean group $\text{SE}(2)$, parameterized by the transformation matrix $\mathbf{T} \in \mathbb{R}^{3 \times 3}$:

$$\mathbf{T} = \begin{bmatrix} \cos \Delta\varphi & -\sin \Delta\varphi & \Delta x \\ \sin \Delta\varphi & \cos \Delta\varphi & \Delta y \\ 0 & 0 & 1 \end{bmatrix}.$$

To ensure accurate pose correction, we minimize the squared Euclidean alignment error:

$$\min \mathcal{L} = \|\mathbf{TP}_0 - \mathbf{P}_{\text{gt}}\|_2^2,$$

where \mathbf{T} is inferred by the end-to-end differentiable network. localization accuracy.

Overview. As depicted in Fig. 2, U-ViLAR comprises two key components: Perceptual Uncertainty-guided (PU-Guided) Association and Localization Uncertainty-guided (LU-Guided) Registration. The LU-Guided Registration component enhances the localization output by utilizing the coarse pose and distribution generated by the PU-Guided Association.

3.1. BEV Feature Extraction and Fusion

As shown in the upper part of Fig. 2, to establish correspondences between images and maps for accurate localization, we first extract features from both image and map inputs, and align them to the BEV space. Then, feature fusion is performed within this unified representation.

Visual Encoder. For monocular or multi-view images $\{I_i | i = 1, 2, \dots, N\}$, we feed them into a shared backbone

network (e.g., ResNet [14]) to obtain $\{F_i^v | i = 1, 2, \dots, N\}$, where $F_i^v \in \mathbb{R}^{H_v \times W_v \times C_v}$ represents the feature map of the i -th view, with H_v and W_v denoting the height and width of the extracted features, respectively. Then, following the approach of BEVFormer [23], we apply a view transformation to the extracted visual features and project them into the BEV space, resulting in the visual BEV features $\mathbf{F}_v^{\text{BEV}} \in \mathbb{R}^{H_v^{\text{BEV}} \times W_v^{\text{BEV}} \times C_v^{\text{BEV}}}$, where the visual BEV space size is $H_v^{\text{BEV}} \times W_v^{\text{BEV}}$.

Map Encoder. Our method supports HD maps or navigation maps as input, with similar map processing strategies adopted in previous research, such as [39, 49]. When employing HD maps, we utilize the high-definition map data provided by the respective datasets. For navigation maps, OpenStreetMap [13] (OSM) serves as the data source. Various elements (lanes, curbs, etc.) are rasterized with a fixed sampling distance Δ (e.g., 25 cm/pixel), resulting in $I_{\text{map}} \in \mathbb{R}^{H_m \times W_m \times N_m}$, where $H_m \times W_m$ represents the rasterized result of a particular element, and N_m is the number of elements in the map. The rasterized map image I_{map} is then passed through a U-Net-like backbone [35] to extract the map features $\mathbf{F}_m^{\text{BEV}} \in \mathbb{R}^{H_m^{\text{BEV}} \times W_m^{\text{BEV}} \times C_m^{\text{BEV}}}$, where the map BEV space size is $H_m^{\text{BEV}} \times W_m^{\text{BEV}}$.

Cross-Modality Fusion. We perform cross-modal fusion by alternately applying self-attention (SA) and cross-attention (CA) to integrate visual BEV feature $\mathbf{F}_v^{\text{BEV}}$ and map BEV feature $\mathbf{F}_m^{\text{BEV}}$, resulting in the enhanced features $\mathbf{F}_v^{\prime\text{BEV}}$ and $\mathbf{F}_m^{\prime\text{BEV}}$:

$$\mathbf{F}_v^{\prime\text{BEV}} = \text{CA}(\text{SA}(\mathbf{F}_v^{\text{BEV}}), \text{SA}(\mathbf{F}_m^{\text{BEV}})), \quad (1)$$

$$\mathbf{F}_m^{\prime\text{BEV}} = \text{CA}(\text{SA}(\mathbf{F}_m^{\text{BEV}}), \text{SA}(\mathbf{F}_v^{\text{BEV}})), \quad (2)$$

where $\text{SA}(\cdot)$ and $\text{CA}(Q, K)$ represent self-attention and cross-attention with query-key pairs.

3.2. Perceptual Uncertainty-guided Association

Overview. When associating semantic elements between vision and maps, visual inputs often suffer from perceptual degradation, such as occlusions of key semantic elements. To tackle this issue, we propose a method that models perceptual uncertainty to guide the cross-modal association between visual features and map features in BEV space. Specifically, we supervise the perceptual uncertainty of $\mathbf{F}_v^{\prime\text{BEV}}$, which supports perception tasks and facilitates the generation of BEV perceptual uncertainty, as illustrated in Fig. 2. We then incorporate this perceptual uncertainty into the association modeling between $\mathbf{F}_v^{\prime\text{BEV}}$ and $\mathbf{F}_m^{\prime\text{BEV}}$, creating a perceptual uncertainty-aware similarity matrix. Furthermore, to enhance the model’s ability to establish fine-grained cross-modal associations for spatially close points within local regions, we sample local windows from $\mathbf{F}_v^{\prime\text{BEV}}$ and $\mathbf{F}_m^{\prime\text{BEV}}$, using contrastive learning to supervise the associations within these sampled windows.

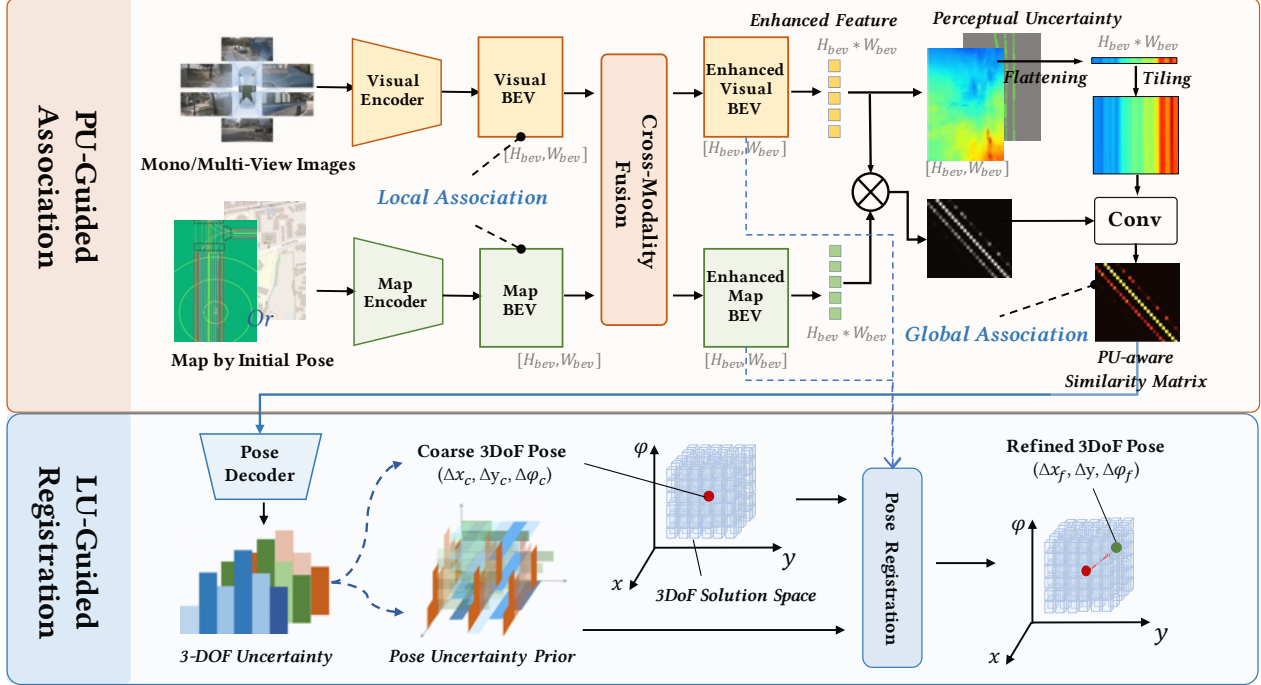


Figure 2. **An overview of the proposed U-VILAR.** First, we extract features from image and map inputs, then align these features into BEV space to obtain visual and map features. These features undergo cross-modal fusion to enhance visual and map features (Sec. 3.1). During the Perceptual Uncertainty-guided (PU-Guided) Association phase (Sec. 3.2), we construct a similarity matrix from the features above and refine it through probabilistic guidance using perceptual uncertainty derived from visual features, yielding a Perceptual Uncertainty-aware (PU-aware) similarity matrix. During the Localization Uncertainty-guided (LU-Guided) Registration phase, this matrix is processed by the pose decoder to yield a coarse pose distribution and a coarse pose. These outputs serve as the pose uncertainty prior and the center of the solution space for Pose Registration. Finally, precise poses are obtained by registering the enhanced visual-map BEV (Sec. 3.3).

Perceptual Uncertainty. We enhance the feature learning by incorporating road structure-aware supervision with uncertainty prediction on $\mathbf{F}_v^{\text{BEV}}$. Inspired by [48], we estimate a pixel-wise uncertainty field $\mathbf{U}_p \in \mathbb{R}^{H_v^{\text{BEV}} \times W_v^{\text{BEV}}}$ to guide the feature refinement. The uncertainty loss is formulated as:

$$\mathcal{L}_p = \exp(-\mathbf{U}_p) \|\mathbf{F} - \hat{\mathbf{F}}\|_1 + 2\mathbf{U}_p, \quad (3)$$

where $\hat{\mathbf{F}}$ denotes the BEV feature estimate refined by road structure segmentation prediction, and \mathbf{U}_p models the heteroscedasticity in feature prediction. This loss dynamically adjusts reconstruction weights through the $\exp(-\mathbf{U}_p)$ term, relaxing constraints in high-uncertainty regions (e.g., occlusion boundaries) while maintaining strict feature alignment in confident areas.

Global Association. By computing the similarity matrix $\mathbf{S} \in \mathbb{R}^{(H_v^{\text{BEV}} W_v^{\text{BEV}}) \times (H_m^{\text{BEV}} W_m^{\text{BEV}})}$ between the visual BEV feature map $\mathbf{F}_v^{\text{BEV}}$ and the map BEV feature map $\mathbf{F}_m^{\text{BEV}}$, we model the cross-modal similarity relationship:

$$\mathbf{S}(i, j) = \langle \mathbf{F}_v^{\text{BEV}}(i), \mathbf{F}_m^{\text{BEV}}(j) \rangle, \quad (4)$$

where $i \in \{1, \dots, H_v^{\text{BEV}} W_v^{\text{BEV}}\}$ and $j \in \{1, \dots, H_m^{\text{BEV}} W_m^{\text{BEV}}\}$ represent the spatial unit indices in the visual and map BEV, respectively.

To incorporate perceptual uncertainty, we begin by flattening the 2D uncertainty mask $\mathbf{U}_p \in \mathbb{R}^{H_v^{\text{BEV}} \times W_v^{\text{BEV}}}$ into a 1D vector $\mathbf{U}_p^{\text{flat}} \in \mathbb{R}^{H_v^{\text{BEV}} W_v^{\text{BEV}}}$. This flattened vector is then tiled to align with the spatial dimensions of \mathbf{S} , resulting in a tiled matrix $\mathbf{U}_p^{\text{tile}} \in \mathbb{R}^{(H_v^{\text{BEV}} W_v^{\text{BEV}}) \times (H_m^{\text{BEV}} W_m^{\text{BEV}})}$.

Subsequently, we perform a channel-wise concatenation of the original similarity matrix \mathbf{S} with the tiled uncertainty matrix $\mathbf{U}_p^{\text{tile}}$. This concatenated result is then processed through a CNN, which consists of a lightweight network with a 1×1 convolutional layer and ReLU activation, ultimately generating the perceptual uncertainty-aware similarity matrix $\mathbf{S}_{\text{uncert}}$. The final association distribution $\mathbf{P} \in \mathbb{R}^{(H_v^{\text{BEV}} W_v^{\text{BEV}}) \times (H_m^{\text{BEV}} W_m^{\text{BEV}})}$ is computed by applying Soft-max normalization to $\mathbf{S}_{\text{uncert}}$:

$$\mathbf{P}_{i,j} = \frac{\exp(\mathbf{S}_{\text{uncert}}(i, j))}{\sum_{k=1}^{H_m^{\text{BEV}} W_m^{\text{BEV}}} \exp(\mathbf{S}_{\text{uncert}}(i, k))}. \quad (5)$$

As shown in Fig. 3, to avoid quantization errors caused by supervision with a hard binary mask, we construct a similarity soft supervision matrix $\mathbf{G} \in \mathbb{R}^{(H_v^{\text{BEV}} W_v^{\text{BEV}}) \times (H_m^{\text{BEV}} W_m^{\text{BEV}})}$

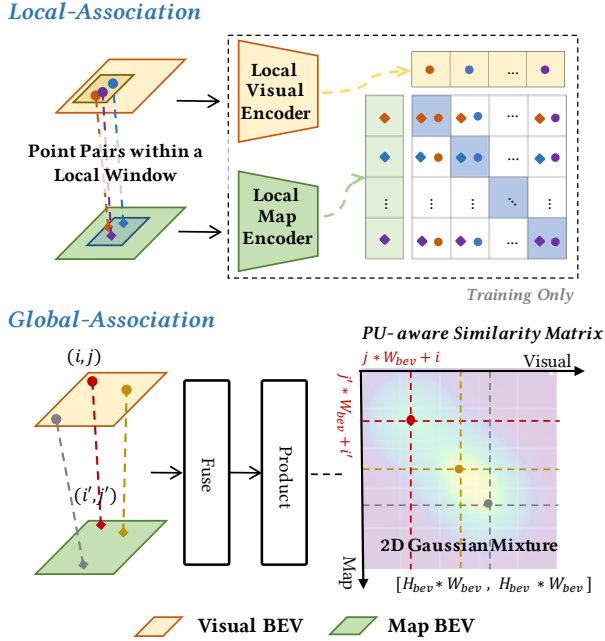


Figure 3. **Illustration of Local Association and Global Association.** The BEV features in the upper and lower parts are the original and the enhanced ones, respectively.

using a multivariate Gaussian distribution:

$$\mathbf{G}_{i,j} = \begin{cases} \exp\left(-\frac{d^2(i,j)}{2\sigma_i^2}\right) & d(i,j) \leq 3\sigma_i \\ 0 & \text{otherwise,} \end{cases} \quad (6)$$

where $d(i,j)$ represents the geometric offset between the two spatial units, and σ_i is an adaptive smoothing factor. For each visual unit i , normalization is performed along the map dimension to obtain $\tilde{\mathbf{G}}_{i,j}$. The supervision loss is defined as the cross-entropy between the predicted association distribution \mathbf{P} and the soft target $\tilde{\mathbf{G}}$:

$$\mathcal{L}_{\text{GM}} = - \sum_{i=1}^{H_v^{\text{BEV}} W_v^{\text{BEV}}} \sum_{j=1}^{H_m^{\text{BEV}} W_m^{\text{BEV}}} \tilde{\mathbf{G}}_{i,j} \log \mathbf{P}_{i,j}. \quad (7)$$

Local Association. Initially, we leverage the pose ground truth to create spatial correspondences between the visual BEV features, $\mathbf{F}_v^{\text{BEV}}$, and the map BEV features, $\mathbf{F}_m^{\text{BEV}}$. Following this, \mathbf{M} anchor points are uniformly distributed across the space, with each anchor overseeing a local window of dimensions $[\mathbf{H}_p, \mathbf{W}_p]$. For each of these anchors, \mathbf{K} pairs of ground-truth points are sampled, with features $\mathbf{F}_i^{\text{map}}$ and $\mathbf{F}_i^{\text{vis}}$ extracted by train-only encoders. Subsequently, a symmetric local similarity matrix $\mathbf{S} \in \mathbb{R}^{\mathbf{K} \times \mathbf{K}}$ is constructed in the BEV local space using contrastive learning principles, where elements are computed as:

$$\mathbf{S}_{ij} = \frac{\mathbf{F}_i^{\text{vis}} \cdot \mathbf{F}_j^{\text{map}}}{\|\mathbf{F}_i^{\text{vis}}\| \|\mathbf{F}_j^{\text{map}}\|}, \quad \forall i, j \in \{1, \dots, \mathbf{K}\}. \quad (8)$$

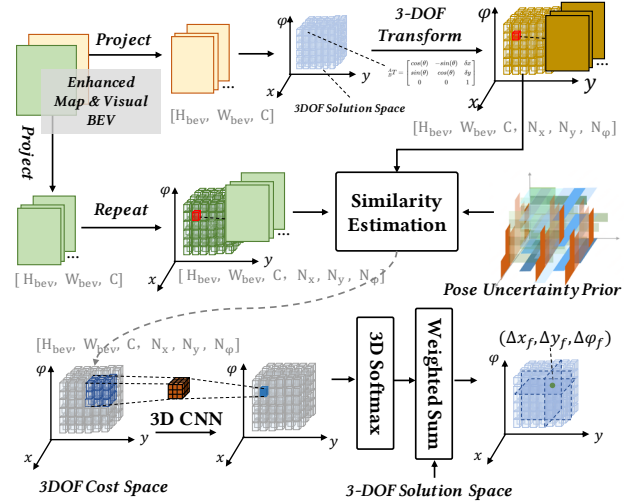


Figure 4. **Illustration of the Pose Registration.** The solution space is constructed centered around the coarse pose, and the precise pose is obtained by estimating the probability of each candidate pose by the coarse prior.

The similarity of positive sample pairs is optimized via a symmetric cross-entropy loss:

$$\mathcal{L}_{\text{LM}} = \frac{1}{2\mathbf{K}} \sum_{i=1}^{\mathbf{K}} \left[-\log \frac{e^{\mathbf{S}_{ii}}}{\sum_{j=1}^{\mathbf{K}} e^{\mathbf{S}_{ij}}} - \log \frac{e^{\mathbf{S}_{ii}}}{\sum_{j=1}^{\mathbf{K}} e^{\mathbf{S}_{ji}}} \right]. \quad (9)$$

3.3. Localization Uncertainty-guided Registration

Overview. Most second-stage coarse-to-fine localization approaches rely heavily on the initial coarse pose input, yielding refined results that remain closely tied to the initial estimation. This oversight neglects potential degeneracy in specific degrees of freedom or multimodal distributions, where poor-quality coarse poses would render subsequent local regression meaningless. To address this, we construct the pose solution space not only from the coarse pose but also model a 3D joint probability distribution from the coarse 3DoF pose estimates, enabling error correction through probabilistic-guided pose registration and weighted fusion.

Localization Uncertainty. As shown in the lower part of Fig. 2, we regress 3DoF probability distributions via a pose decoder from the perceptual uncertainty-aware similarity matrix $\mathcal{S}_{\text{uncert}}$. Specifically, we discretize each DoF: $x \in [x_{\min}^c, x_{\max}^c]$ into N_x bins, $y \in [y_{\min}^c, y_{\max}^c]$ into N_y bins, and orientation $\phi \in [\phi_{\min}^c, \phi_{\max}^c]$ into N_ϕ bins. The decoder outputs independent probability distributions $\mathbf{p}_x \in \mathbb{R}^{N_x}$, $\mathbf{p}_y \in \mathbb{R}^{N_y}$, and $\mathbf{p}_\phi \in \mathbb{R}^{N_\phi}$ (with $\sum \mathbf{p}_* = 1$). Supervision is provided by Gaussian distributions centered at ground truth with standard deviations controlling distribution widths, normalized to form probability targets.

The uncertainty for each DoF (lateral x , longitudinal y , and rotational φ) is quantified via Shannon entropy:

$$U_d = - \sum_{n=1}^{N_d} \mathbf{p}_d^{(n)} \log \mathbf{p}_d^{(n)}, \quad d \in \{x, y, \varphi\} \quad (10)$$

where N_d denotes bin count for DoF d , and $\mathbf{p}_d^{(n)}$ represents the n -th bin probability. This generalized entropy formulation preserves DoF-specific parameters (e.g., varying N_x, N_y, N_φ) while maintaining physical consistency with individual uncertainty metrics.

Coarse Pose Regression and 3D Joint Distribution. The 3DoF distributions are concatenated and fed to an MLP to regress coarse pose estimates (x_c, y_c, φ_c) . Simultaneously, we construct a joint probability space via Cartesian product:

$$\mathbf{P}_{\text{uncert}}(i, j, k) = \mathbf{p}_x^{(i)} \cdot \mathbf{p}_y^{(j)} \cdot \mathbf{p}_\varphi^{(k)}, \quad \mathbf{P}_{\text{uncert}} \in \mathbb{R}^{N_x \times N_y \times N_\varphi}. \quad (11)$$

Localization Uncertainty-Guided Pose Registration. As shown in Fig. 4, based on the coarse pose (x_c, y_c, φ_c) and joint prior $\mathbf{P}_{\text{uncert}}$, we define a 3D solution space Ω centered around the coarse pose, with ranges $[x_c \pm \Delta_x]$, $[y_c \pm \Delta_y]$, and $[\varphi_c \pm \Delta_\varphi]$. This space is discretized into (H_s, W_s, D_s) candidates, indexed by (i, j, k) , with resolutions $(\delta_x, \delta_y, \delta_\varphi) = (\frac{2\Delta_x}{H_s}, \frac{2\Delta_y}{W_s}, \frac{2\Delta_\varphi}{D_s})$. Consequently, visual features $\mathbf{F}_v^{\text{BEV}}$ undergo 3DoF geometric transformations in solution space Ω :

$$\mathbf{F}_v^T(h, w, c, i, j, k) = \mathcal{T}_{\theta_{i,j,k}}(\mathbf{F}_v^{\text{BEV}}(h, w, c)),$$

$$\theta_{i,j,k} = (x_c - \Delta_x + i\delta_x, y_c - \Delta_y + j\delta_y, \varphi_c - \Delta_\varphi + k\delta_\varphi), \quad (12)$$

where $\mathcal{T}_\theta(\cdot)$ denotes the 3DoF transform operator. Map features $\mathbf{F}_m^{\text{BEV}}$ are aligned and broadcast to match dimensions as \mathbf{F}_m^B . The feature difference tensor \mathbf{D}_{cost} is computed as the L2 norm between the transformed visual features \mathbf{F}_v^T and the aligned map features \mathbf{F}_m^B .

Subsequently, the joint probability $\mathbf{P}_{\text{uncert}}$ is fused with the feature difference tensor \mathbf{D}_{cost} via gating, serving as a prior for the pose registration:

$$\mathbf{D}_{\text{fused}} = \mathbf{D}_{\text{cost}} + \lambda \cdot \text{repeat}(\text{unsqueeze}(\mathbf{P}_{\text{uncert}})). \quad (13)$$

where λ is a learnable parameter. After convolutional processing of $\mathbf{D}_{\text{fused}}$, the cost tensor in cost space tensor $\mathbf{C} \in \mathbb{R}^{H_s \times W_s \times D_s}$ is obtained, and the refined pose (x_f, y_f, φ_f) is obtained via softmax-weighted fusion:

$$(x_f, y_f, \varphi_f) = \sum_{i,j,k} \sigma(\mathbf{C} + \gamma \mathbf{P}_{\text{uncert}})_{i,j,k} \cdot (x_c - \Delta_x + i\delta_x, y_c - \Delta_y + j\delta_y, \varphi_c - \Delta_\varphi + k\delta_\varphi), \quad (14)$$

where γ controls prior strength and $\sigma(\cdot)$ denotes 3D softmax. The parameter γ dynamically modulates the balance

of weights between the probabilistic coarse pose prior and data-driven signals during pose refinement, enabling the model to adaptively adjust its reliance on prior knowledge according to the uncertainty inherent in the input scene.

4. Experiment

4.1. Experimental Setup

Datasets. We evaluate our method on three datasets: nuScenes [5], a widely used autonomous driving dataset containing 1,000 scenarios with over 28,000 frames for training and 6,000 frames for validation; KITTI [11], which includes 39.2 km of visual odometry sequences; and our self-collected SRoad dataset, which contains over 500,000 frames and features more complex road structures: over 60% of the scenarios present specific challenges, such as intersections, merging/diverging zones, congested areas, or areas under viaducts (details in Appendix).

Tasks, Metrics and Comparison Methods. We comprehensively compared previous studies across various datasets and map sources. The localization tasks are divided into two categories: (a) **Fine-grained Localization:** We conducted experiments using the nuScenes and SRoad datasets, utilizing their respective HD maps, and employed an ICP method as the rule-based baseline (details in Appendix). Our method was compared with BEV-Locator and OrienterNet, using MAE and RMSE to evaluate localization performance. (b) **Large-scale Relocalization:** We used nuScenes, KITTI, and SRoad datasets with OSM map input. Following Shi et al. [41], we computed recall rates for Lateral, Longitudinal, and Orientation at fixed thresholds. On nuScenes, we evaluated recall for position and orientation to align with metrics of previous methods.

Implementation Details. Aligned with previous work, in fine-grained localization, small random transformations (rotation $\theta \in [-2^\circ, 2^\circ]$, translation $t \in [-2\text{m}, 2\text{m}]$) are applied to HD maps to simulate GPS noise, followed by extracting a $120\text{m} \times 120\text{m}$ search region centered on the ego vehicle. For relocalization, larger perturbations (rotation $\theta \in [-30^\circ, 30^\circ]$, translation $t \in [-30\text{m}, 30\text{m}]$) are introduced to address significant pose deviations, processing a $128\text{m} \times 128\text{m}$ search area on the navigation map (details in Appendix).

4.2. Results

Fine-grained Localization. Table 1 presents the experimental results of centimeter-level localization tasks using different datasets and their corresponding HD maps. The MAE and RMSE metrics demonstrate the superiority of our approach. Notably, on the nuScenes dataset, we significantly reduced horizontal and vertical MAE compared to BEV-Locator, with an 85.3% decrease in Orientation MAE (0.075 v.s. 0.510). Compared to the monocular version of OrienterNet, our errors were comprehensively reduced,

Methods	Inputs	Lateral Error ↓		Longitudinal Error ↓		Orientation Error ↓	
		MAE(m)	RMSE(m)	MAE(m)	RMSE(m)	MAE(°)	RMSE(°)
BEV-Locator-M	nuScenes + HD map	0.076	-	0.178	-	0.510	-
Ours-M	nuScenes + HD map	0.040	0.049	0.140	0.158	0.075	0.089
OrionerNet-S	nuScenes + HD map	0.079	0.154	0.279	0.473	0.114	0.143
Ours-S	nuScenes + HD map	0.069	0.134	0.223	0.324	0.092	0.105
ICP-based-M	SRoad + HD map	0.204	0.320	0.614	1.106	0.186	0.204
Ours-M	SRoad + HD map	0.110	0.136	0.284	0.322	0.090	0.124
OrionerNet-S	SRoad + HD map	0.186	0.241	0.492	0.724	0.160	0.245
Ours-S	SRoad + HD map	0.165	0.193	0.390	0.484	0.122	0.154

Table 1. **Centimeter-level localization results on nuScenes and SRoad using their respective HD maps as input.** We use **bold** font to highlight the best results. S and M represent monocular and multi-view inputs, respectively.

Methods	Inputs	Lateral Recall@Xm ↑			Longitudinal Recall@Xm ↑			Orientation Recall@X° ↑		
		1m	3m	5m	1m	3m	5m	1°	3°	5°
OrionerNet-S	KITTI + OSM	51.26	84.77	91.81	22.39	46.79	57.81	20.41	52.24	73.53
Ours-S	KITTI + OSM	69.12	91.25	93.68	32.04	63.00	70.20	64.92	94.84	97.44
OrionerNet-S	SRoad + OSM	35.23	76.38	84.51	15.20	35.40	48.91	16.21	40.12	62.77
Ours-S	SRoad + OSM	52.90	86.20	88.03	27.94	45.53	55.84	49.91	82.50	86.01

Table 2. **Localization results on KITTI and SRoad dataset using OSM as the map input.** We use **bold** font to highlight the best results. S and M represent monocular and multi-view inputs, respectively.

Methods	Position Recall@Xm ↑			Orientation Recall@X° ↑		
	1m	3m	5m	1°	3°	5°
OrionerNet-S	5.83	18.92	52.83	32.13	41.56	65.63
MapLocNet-S	8.96	27.05	64.57	40.36	65.31	89.66
Ours-S	23.98	39.43	68.73	44.40	70.02	91.39
U-BEV [7]-M	16.89	41.60	71.33	-	-	-
MapLocNet-M	20.10	45.54	77.70	58.61	84.10	96.23
Ours-M	34.53	56.21	82.21	60.32	86.28	97.00

Table 3. **Localization results on the nuScenes dataset using OSM as the map input.** We compared our method with existing approaches based on both mono-view and multi-view. Similarly, we use **bold** font to highlight the best results. S and M represent monocular and multi-view inputs, respectively.

particularly the difference in RMSE, reflecting the stability of our localization method. Our method shows significant advantages over traditional ICP-based industrial standard methods for the challenging SRoad dataset.

Large-scale Relocalization. As shown in Table 2 and Table 3, we compared our method with previous approaches on the KITTI, nuScenes, and SRoad datasets to evaluate large-scale relocalization capabilities using OSM as the map input. Our method consistently outperforms existing approaches when the threshold is set to 1m, 3m, and 5m, demonstrating its robust capability in both coarse relocation and fine-grained localization.

Runtime Analysis. We deploy our model on an NVIDIA V100 GPU, achieving an impressive 28 frames per second (FPS). This high efficiency stems from our training-only optimizations, which enhance model performance with-

out introducing additional latency. On NVIDIA Orin, a widely used autonomous driving platform, we apply TensorRT INT8 quantization to the BEV encoder, optimizing efficiency and achieving a 15 FPS runtime for the entire model.

4.3. Ablation Study

To assess the effectiveness of each component of our method, we performed a series of ablation experiments using the nuScenes dataset along with its corresponding HD map. The experimental results on other datasets and our experiments using a Kalman filter to validate the value of localization uncertainty output further are provided in **Appendix**.

PU-Guided Association and LU-Guided Registration. We conducted experiments using multi-view images as shown in Table 4. Comparing S2 and S3 with S1 shows that PU-Guided Association significantly impacts localization more than LU-Guided Registration. Removing all components (S4) results in severe performance degradation. These findings underscore the necessity of combining PU-Guided Association and LU-Guided Registration to optimize localization.

Local Association, Global Association and Perceptual Uncertainty. As shown in Table 5, when Perceptual Uncertainty is removed and the original Similarity Matrix is used instead of the PU-aware Similarity Matrix, a significant increase in localization error is observed, underscoring the crucial role of Perceptual Uncertainty in the process.

	Assoc.	Reg.	Lat. ↓ MAE(m)	Lon. ↓ MAE(m)	Ori. ↓ MAE(°)
S1	✓	✓	0.040	0.140	0.075
S2		✓	0.058	0.157	0.108
S3	✓		0.047	0.149	0.087
S4			0.064	0.160	0.360

Table 4. **Ablation experiments on the key components of our method using the nuScenes dataset and HD map.** ‘Assoc.’ and ‘Reg.’ denote PU-Guided Association and LU-Guided Registration, respectively. ‘Lat.’, ‘Lon.’, and ‘Ori.’ stand for Lateral, Longitudinal, and Orientation, respectively.

	LA.	GA.	PU.	Lat. ↓ MAE(m)	Lon. ↓ MAE(m)	Ori. ↓ MAE(°)
S1	✓	✓	✓	0.040	0.140	0.075
S2	✓	✓		0.050	0.149	0.094
S3		✓	✓	0.043	0.144	0.081

Table 5. **Ablation experiments of the key components of PU-Guided Association on the nuScenes dataset and HD map.** ‘LA.’, ‘GA.’, ‘PU.’ represent Local Association, Global Association, and Perceptual Uncertainty, respectively.

	Lat. ↓		Lon. ↓		Ori. ↓	
	M.(m)	R.(m)	M.(m)	R.(m)	M.(°)	R.(°)
baseline	0.040	0.049	0.140	0.158	0.075	0.089
w/o PDP.	0.042	0.054	0.144	0.184	0.079	0.099

Table 6. **Ablation results of pose distribution prior of LU-Guided Registration on the nuScenes dataset and HD map.** ‘PDP.’ represent Pose Distribution Prior and ‘M.’, ‘R.’ represent MAE and RMSE, respectively.

Conversely, Local Association has a relatively small impact on localization accuracy.

Pose Uncertainty Prior. Based on the comparison of the two rows in Table 6, it is clear that omitting the Pose Uncertainty Prior as input information for Registration results in some deterioration of our primary metric, MAE, reflecting a decline in localization performance. Notably, RMSE experiences an even more pronounced degradation. This aligns with the fundamental design purpose of the Pose Uncertainty Prior, which is intended to be particularly effective in the less common non-unimodal scenarios within the dataset.

4.4. Qualitative Analysis

Visualization of Perceptual Uncertainty and Similarity Matrix.

As shown in Fig. 5, red-circled curb perception results (green polylines) mispredict a left turn as straight, aligning with the highest perceptual uncertainty. The ground truth and predicted results of the PU-aware Similarity Matrix are shown on the right, with the horizontal and vertical axes

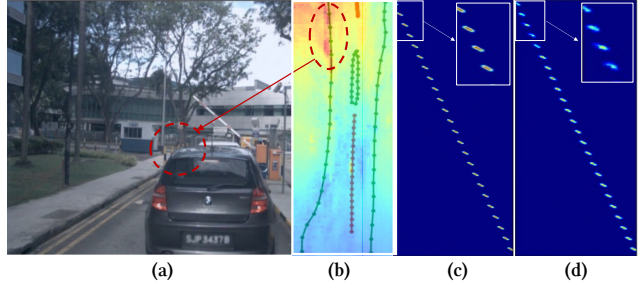


Figure 5. **Visualization on the nuScenes validation set.** From left to right: (a) Front view, (b) Road-structure predictions overlaid with a BEV uncertainty heatmap, where red circles highlight regions of high uncertainty, (c) Ground truth and (d) Inference results of the PU-aware Similarity Matrix.

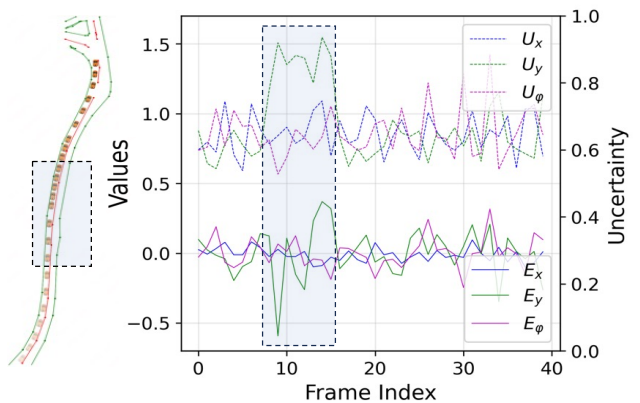


Figure 6. **Trajectory segment from nuScenes validation set (left) and per-frame localization results (right).** E_x, E_y, E_ϕ : lateral, longitudinal, orientation errors; U_x, U_y, U_ϕ : lateral, longitudinal, orientation uncertainties.

representing the visual BEV space and map BEV space, respectively. In regions with poor association predictions (upper part), the Gaussian kernel is weaker and less accurate, indicating inferior association predictions for distant areas (due to occlusion).

Consistency between Localization Uncertainty and Localization Quality.

Fig. 6 presents the single-frame inference results for a clip of the nuScenes validation set. It can be observed that the 3DoF errors remain close to zero in most cases, with a positive correlation between uncertainty and localization error. Notably, within the blue-boxed region, the longitudinal localization error is generally larger and more unstable, while the longitudinal uncertainty is significantly higher than usual. This phenomenon is caused by the reduced longitudinal constraints in this region, leading to a degeneracy issue. The above results highlight the quality and value of uncertainty prediction.

5. Conclusion

This paper presents a novel uncertainty-aware localization network that integrates the advantages of association and registration, demonstrating strong performance across various localization tasks. We thoughtfully design global and local association constraints, where the association is guided by perception uncertainty. Based on the pose distribution and uncertainty estimated by the above module, we perform pose registration to obtain precise localization. Our approach shows significant advantages over existing methods across multiple datasets. Future work will focus on optimizing localization accuracy in extremely challenging scenarios (e.g., with very limited observations) while enhancing the model’s generalization ability to achieve a unified model capable of supporting diverse datasets and various maps.

References

- [1] Alexandre Alahi, Raphael Ortiz, and Pierre Vanderghenst. Freak: Fast retina keypoint. In *CVPR*, pages 510–517, 2012. [1](#)
- [2] Ioan Andrei Bârsan, Shenlong Wang, Andrei Pokrovsky, and Raquel Urtasun. Learning to localize using a lidar intensity map. 2018. [1](#)
- [3] Herbert Bay, Tinne Tuytelaars, and Luc Van Gool. Surf: Speeded up robust features. In *ECCV*, pages 404–417. Springer, 2006. [1](#)
- [4] Mathias Bürki, Lukas Schaupp, Marcin Dymczyk, Renaud Dubé, Cesar Cadena, Roland Siegwart, and Juan Nieto. Vizard: Reliable visual localization for autonomous vehicles in urban outdoor environments. pages 1124–1130. IEEE, 2019. [1](#)
- [5] Holger Caesar, Varun Bankiti, Alex H Lang, Sourabh Vora, Venice Erin Liong, Qiang Xu, Anush Krishnan, Yu Pan, Giancarlo Baldan, and Oscar Beijbom. nuscenes: A multimodal dataset for autonomous driving. In *CVPR*, pages 11621–11631, 2020. [6](#)
- [6] Michael Calonder, Vincent Lepetit, Christoph Strecha, and Pascal Fua. Brief: Binary robust independent elementary features. In *ECCV*, pages 778–792. Springer, 2010. [1](#)
- [7] Andrea Boscolo Camiletto, Alfredo Bochicchio, Alexander Liniger, Dengxin Dai, and Abel Gawel. U-bev: Height-aware bird’s-eye-view segmentation and neural map-based relocalization. 2024. [7](#)
- [8] Kuangyi Chen, Huai Yu, Wen Yang, Lei Yu, Sebastian Scherer, and Gui-Song Xia. I2d-loc: Camera localization via image to lidar depth flow. *ISPRS Journal of Photogrammetry and Remote Sensing*, 194:209–221, 2022. [3](#)
- [9] Daniel DeTone, Tomasz Malisiewicz, and Andrew Rabinovich. Superpoint: Self-supervised interest point detection and description. pages 224–236, 2018. [1](#), [2](#)
- [10] Florian Fervers, Sebastian Bullinger, Christoph Bodensteiner, Michael Arens, and Rainer Stiefelhagen. Uncertainty-aware vision-based metric cross-view geolocalization. In *CVPR*, pages 21621–21631, 2023. [2](#)
- [11] Andreas Geiger, Philip Lenz, Christoph Stiller, and Raquel Urtasun. Vision meets robotics: The KITTI dataset. In *CVPR*, 2013. [6](#)
- [12] Shi Gong, Xiaoqing Ye, Xiao Tan, Jingdong Wang, Errui Ding, Yu Zhou, and Xiang Bai. Gitnet: Geometric prior-based transformation for birds-eye-view segmentation. In *ECCV*, 2022. [2](#)
- [13] Mordechai Haklay and Patrick Weber. Openstreetmap: User-generated street maps. *IEEE Pervasive computing*, 7(4):12–18, 2008. [2](#), [3](#)
- [14] Kaiming He, X. Zhang, Shaoqing Ren, and Jian Sun. Deep residual learning for image recognition. *Proceedings of the IEEE Conference on Computer Vision and Pattern Recognition (CVPR)*, pages 770–778, 2016. [3](#)
- [15] Yuzhe He, Shuang Liang, Xiaofei Rui, Chengying Cai, and Guowei Wan. Egovm: Achieving precise ego-localization using lightweight vectorized maps. 2024. [3](#)
- [16] Junjie Huang, Guan Huang, Zheng Zhu, and Dalong Du. Bevdet: High-performance multi-camera 3d object detection in bird-eye-view. *arXiv preprint arXiv:2112.11790*, 2021. [2](#)
- [17] Alex Kendall, Matthew Grimes, and Roberto Cipolla. Posenet: A convolutional network for real-time 6-dof camera relocalization. In *ICCV*, 2015. [2](#)
- [18] Ted Lentsch, Zimin Xia, Holger Caesar, and Julian FP Kooij. Slicematch: Geometry-guided aggregation for cross-view pose estimation. In *CVPR*, pages 17225–17234, 2023. [2](#)
- [19] Jesse Levinson, Michael Montemerlo, and Sebastian Thrun. Map-based precision vehicle localization in urban environments. volume 4, page 1, 2007. [2](#)
- [20] Jesse Levinson and Sebastian Thrun. Robust vehicle localization in urban environments using probabilistic maps. pages 4372–4378, May 2010. [2](#)
- [21] Yin hao Li, Zheng Ge, Guanyi Yu, Jinrong Yang, Zengran Wang, Yukang Shi, Jianjian Sun, and Zeming Li. Bevdepth: Acquisition of reliable depth for multi-view 3d object detection. In *AAAI*, volume 37, pages 1477–1485, 2023. [2](#)
- [22] Yunpeng Li, Noah Snaveley, Daniel P Huttenlocher, and Pascal Fua. Worldwide pose estimation using 3d point clouds. *Large-Scale Visual Geo-Localization*, pages 147–163, 2016. [2](#)
- [23] Zhiqi Li, Wenhai Wang, Hongyang Li, Enze Xie, Chonghao Sima, Tong Lu, Yu Qiao, and Jifeng Dai. Bevformer: Learning bird’s-eye-view representation from multi-camera images via spatiotemporal transformers. In *Computer Vision—ECCV 2022: 17th European Conference, Tel Aviv, Israel, October 23–27, 2022, Proceedings, Part IX*, pages 1–18. Springer, 2022. [2](#), [3](#)
- [24] Philipp Lindenberger, Paul-Edouard Sarlin, Viktor Larsson, and Marc Pollefeys. Pixel-perfect structure-from-motion with featuremetric refinement. In *ICCV*, pages 5987–5997, 2021. [2](#)
- [25] Chris Linegar, Winston Churchill, and Paul Newman. Work smart, not hard: Recalling relevant experiences for vast-scale but time-constrained localisation. pages 90–97, 2015. [1](#)
- [26] Yong Liu, Lingjing Fan, Sen Xiang, Jiaqi Pan, Mingliang Cheng, Jinhui Tang, Fei Zhao, Zilei Wang, and Qingxiong Zhao. Gift: A real-time and scalable 3d spatial feature descriptor. In *CVPR*, pages 6783–6791, 2017. [1](#)

- [27] Yingfei Liu, Tiancai Wang, Xiangyu Zhang, and Jian Sun. Petr: Position embedding transformation for multi-view 3d object detection. In *ECCV*, pages 531–548, 2022. 2
- [28] Yicheng Liu, Tianyuan Yuan, Yue Wang, Yilun Wang, and Hang Zhao. Vectormapnet: End-to-end vectorized hd map learning. pages 22352–22369, 2023. 2
- [29] David G Lowe. Distinctive image features from scale-invariant keypoints. *IJCV*, 60(2):91–110, 2004. 1
- [30] Pilailuck Panphattarasap and Andrew Calway. Automated map reading: image based localisation in 2-d maps using binary semantic descriptors. pages 6341–6348, 2018. 2
- [31] Jan-Hendrik Pauls, Kürsat Petek, Fabian Poggenhans, and Christoph Stiller. Monocular localization in hd maps by combining semantic segmentation and distance transform. In *2020 IEEE/RSJ International Conference on Intelligent Robots and Systems (IROS)*, pages 4595–4601. IEEE, 2020. 2
- [32] Jonah Philion and Sanja Fidler. Lift, splat, shoot: Encoding images from arbitrary camera rigs by implicitly unprojecting to 3d. In *ECCV*, pages 194–210, 2020. 2
- [33] Lennart Reiher, Bastian Lampe, and Lutz Eckstein. A sim2real deep learning approach for the transformation of images from multiple vehicle-mounted cameras to a semantically segmented image in bird’s eye view. In *International Conference on Intelligent Transportation Systems (ITSC)*, pages 1–7, 2020. 2
- [34] Jerome Revaud, Philippe Weinzaepfel, Ceésar de Souza, Noé Pion, Gabriela Csurka, Yann Cabon, and Martin Humenberger. R2d2: Reliable and repeatable detectors and descriptors. In *Advances in Neural Information Processing Systems (NeurIPS)*, pages 12405–12415, 2019. 1, 2
- [35] Olaf Ronneberger, Philipp Fischer, and Thomas Brox. U-net: Convolutional networks for biomedical image segmentation. In *Medical Image Computing and Computer-Assisted Intervention–MICCAI*, pages 234–241, 2015. 3
- [36] Ethan Rublee, Vincent Rabaud, Kurt Konolige, and Gary Bradski. Orb: An efficient alternative to sift or surf. In *2011 International conference on computer vision*, pages 2564–2571. Ieee, 2011. 1
- [37] Noe Samano, Mengjie Zhou, and Andrew Calway. You are here: Geolocation by embedding maps and images. In *ECCV*, pages 502–518. Springer, 2020. 2
- [38] Paul-Edouard Sarlin, Daniel DeTone, Tomasz Malisiewicz, and Andrew Rabinovich. Superglue: Learning feature matching with graph neural networks. In *CVPR*, pages 4938–4947, 2020. 2
- [39] Paul-Edouard Sarlin, Daniel DeTone, Tsun-Yi Yang, Armen Avetisyan, Julian Straub, Tomasz Malisiewicz, Samuel Rota Bulò, Richard Newcombe, Peter Kotschieder, and Vasileios Balntas. Orienternet: Visual localization in 2d public maps with neural matching. In *CVPR*, pages 21632–21642, 2023. 2, 3
- [40] Torsten Sattler, Laura Leal-Taixé, and Marc Pollefeys. Large-scale direct monocular slam. In *Proceedings of the IEEE International Conference on Computer Vision (ICCV)*, 2017. 2
- [41] Yujiao Shi and Hongdong Li. Beyond cross-view image retrieval: Highly accurate vehicle localization using satellite image. In *CVPR*, pages 17010–17020, 2022. 6
- [42] Jamie Shotton, Ben Glocker, Christopher Zach, Shahram Izadi, Antonio Criminisi, and Andrew Fitzgibbon. Scene coordinate regression forests for camera relocalization in rgb-d images. In *Proceedings of the IEEE conference on computer vision and pattern recognition*, pages 2930–2937, 2013. 2
- [43] Jae Kyu Suhr, Jeungin Jang, Daehong Min, and Ho Gi Jung. Sensor fusion-based low-cost vehicle localization system for complex urban environments. 18(5):1078–1086, 2016. 2
- [44] Jiaming Sun, Zehong Shen, Yuang Wang, Hujun Bao, and Xiaowei Zhou. Loftr: Detector-free local feature matching with transformers. In *CVPR*, pages 8922–8931, 2021. 2
- [45] Huayou Wang, Changliang Xue, Yanxing Zhou, Feng Wen, and Hongbo Zhang. Visual semantic localization based on hd map for autonomous vehicles in urban scenarios. pages 11255–11261, 2021. 2
- [46] Yue Wang, Vitor Campagnolo Guizilini, Tianyuan Zhang, Yilun Wang, Hang Zhao, and Justin Solomon. Detr3d: 3d object detection from multi-view images via 3d-to-2d queries. pages 180–191, 2022. 2
- [47] Hang Wu, Zhenghao Zhang, Siyuan Lin, Xiangru Mu, Qiang Zhao, Ming Yang, and Tong Qin. Maplocnet: Coarse-to-fine feature registration for visual re-localization in navigation maps. pages 13198–13205. IEEE, 2024. 2
- [48] Haoqiang Zhang, Wenhan Luo, Wenxiu Yu, and Xiaoyong Yang. Uncertainty-aware learning for video frame interpolation. pages 10543–10554, 2022. 4
- [49] Zhihuang Zhang, Meng Xu, Wenqiang Zhou, Tao Peng, Liang Li, and Stefan Poslad. Bev-locator: An end-to-end visual semantic localization network using multi-view images. In *ECCV*, 2022. 2, 3